









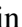











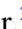











BEBOP V. Homogeneous stellar analysis of potential circumbinary planet hosts

Alix V. Freckelton ¹★, Daniel Sebastian ¹, Annelies Mortier ¹, Amaury H. M. J. Triaud ¹, Pierre F. L. Maxted ², Lorena Acuña ^{3,4}, David J. Armstrong ⁵, Matthew P. Battley ⁶, Thomas A. Baycroft ¹, Isabelle Boisse ³, Vincent Bourrier ⁶, Andres Carmona ⁷, Gavin A. L. Coleman ⁸, Andrew Collier Cameron ⁹, Pía Cortés-Zuleta ^{3,9}, Xavier Delfosse ⁷, Georgina Dransfield ¹, Alison Duck ¹⁰, Thierry Forveille ⁷, Jenni R. French ¹¹, Nathan Hara ⁶, Neda Heidari ¹², Coel Hellier ², Vedad Kunovac ^{5,13}, David V. Martin ¹⁴, Eder Martioli ^{15,16}, James J. McCormac ⁵, Richard P. Nelson ⁸, Lalitha Sairam ^{1,17}, Sérgio G. Sousa ¹⁸, Matthew R. Standing ^{19,20} and Emma Willett ¹

¹*School of Physics & Astronomy, University of Birmingham, Edgbaston, Birmingham B15 2TT, UK*

²*Astrophysics Group, Keele University, Keele, Newcastle, ST5 5BG, UK*

³*Aix-Marseille Université, CNRS, CNES, Institut Origines, LAM, 13388, Marseille, France*

⁴*Max-Planck-Institut für Astronomie, Königstuhl 17, D-69117 Heidelberg, Germany*

⁵*Department of Physics, University of Warwick, Coventry CV4 7AL, UK*

⁶*Observatoire de Genève, Université de Genève, 51 Chemin Pegasi, CH-1290 Versoix, Switzerland*

⁷*Univ. Grenoble Alpes, CNRS, IPAG, F-38000 Grenoble, France*

⁸*Astronomy Unit, School of Physical and Chemical Sciences, Queen Mary University of London, Mile End Road, London, E1 4NS UK*

⁹*Centre for Exoplanet Science, SUPA School of Physics and Astronomy, University of St Andrews, North Haugh, St Andrews KY16 9SS, UK*

¹⁰*Department of Astronomy, The Ohio State University, Columbus, OH 43210, USA*

¹¹*Department of Physics and Astronomy, University of Leicester, University Road, Leicester LE1 7RH, UK*

¹²*Institut d'Astrophysique de Paris, UMR 7095 CNRS Université Pierre et Marie Curie, 98 bis, boulevard Arago, F-75014 Paris, France*

¹³*Centre for Exoplanets and Habitability, University of Warwick, Gibbet Hill Road, Coventry CV4 7AL, UK*

¹⁴*Department of Physics and Astronomy, Tufts University, 574 Boston Avenue, Medford, MA 02155, USA*

¹⁵*Laboratório Nacional de Astrofísica, Rua Estados Unidos 154, 37504-364 Itajubá – MG, Brazil*

¹⁶*Institut d'Astrophysique de Paris, CNRS, UMR 7095, Sorbonne Université, 98 bis bd Arago, F-75014 Paris, France*

¹⁷*Institute of Astronomy, University of Cambridge, Madingley road, Cambridge CB3 0HA, UK*

¹⁸*Instituto de Astrofísica e Ciências do Espaço, Universidade do Porto, CAUP, Rua das Estrelas, P-4150-762 Porto, Portugal*

¹⁹*School of Physical Sciences, The Open University, Walton Hall, Milton Keynes MK7 6AA, UK*

²⁰*European Space Agency (ESA), European Space Astronomy Centre (ESAC), Camino Bajo del Castillo s/n, E-28692 Villanueva de la Cañada, Madrid, Spain*

Accepted 2024 June 1. Received 2024 May 24; in original form 2024 April 25

ABSTRACT

Planets orbiting binary systems are relatively unexplored compared to those around single stars. Detections of circumbinary planets and planetary systems offer a first detailed view into our understanding of circumbinary planet formation and dynamical evolution. The BEBOP (binaries escorted by orbiting planets) radial velocity survey plays a special role in this adventure as it focuses on eclipsing single-lined binaries with an FGK dwarf primary and M dwarf secondary allowing for the highest radial velocity precision using the HARPS and SOPHIE spectrographs. We obtained 4512 high-resolution spectra for the 179 targets in the BEBOP survey which we used to derive the stellar atmospheric parameters using both equivalent widths and spectral synthesis. We furthermore derive stellar masses, radii, and ages for all targets. With this work, we present the first homogeneous catalogue of precise stellar parameters for these eclipsing single-lined binaries.

Key words: techniques: spectroscopic – binaries: eclipsing – binaries: spectroscopic.

1 INTRODUCTION

Circumbinary exoplanets orbit around both stars of a close binary system. The first confirmed systems have been discovered in the

last decade using space-based transit observations e.g. Kepler-16 b (Doyle et al. 2011) and TOI-1338 b (Kostov et al. 2020). Radial velocity (RV) detections of circumbinary planets have proven difficult because of stellar contamination, which has limited the RV precision that can be obtained in double-lined binaries (e.g. Konacki et al. 2010). Nevertheless, Triaud et al. (2022) confirmed the RV signal of the circumbinary planet Kepler-16 b. This was possible

* E-mail: AXF859@student.bham.ac.uk

because the host binary is composed of a solar-type main-sequence star and a low-mass M-dwarf companion. This combination allowed us to treat the primary star spectroscopically as a single-lined star, for which achieving the necessary m s^{-1} precision to detect planetary signals is routinely done (e.g. Faria et al. 2022).

The BEBOP (binaries escorted by orbiting planets) survey for circumbinary planets focuses on the EBLM (eclipsing binaries with low-mass companions) project. Root-mean-square (RMS) scatter in residuals after removing the RV signal caused by the binary can reach down to about 3 m s^{-1} (Standing et al. 2022). The survey has been designed as a blind all-sky survey and its sample was constructed from EBLM binaries detected through transit surveys (e.g. Triaud et al. 2013, 2017; von Boetticher et al. 2019; Lendl et al. 2020). Recently, BEBOP made its first discovery of a circumbinary planet solely based on RV measurements, EBLM J0608-59/TOI-1338/BEBOP-1 c (Standing et al. 2023, BEBOP IV).

Planet parameters, as measured through the transit or RV method, are inherently relative to their host star properties and such properties are often inferred from stellar evolution models (e.g. Dotter et al. 2008). Systematics introduced from different models are thus carried forward to analyses of the other planetary bodies in the system. It is therefore important to use a homogeneous and reliable set of stellar parameters for our BEBOP target stars to minimize any systematics in stellar as well as planetary parameters and ensure the statistical validity of the full survey. Several similar efforts have been done for other surveys (e.g. Sousa et al. 2011; Buchhave et al. 2014).

Throughout the BEBOP survey, we have already assembled a large archive containing thousands of high-resolution spectra of the primary FGK main-sequence stars. These spectra are first and foremost used to build up our RV time series, but they can also be used to measure stellar atmospheric parameters. Furthermore, thanks to the relative brightness of this sample ($V \sim 8\text{--}13$ mag) precise stellar parallaxes from *Gaia* DR3 (Gaia Collaboration et al. 2016, 2023) as well as broad-band photometry from the 2MASS (Skrutskie et al. 2006) and AllWISE (Cutri et al. 2021) surveys are available for all targets. This allows us to use these in combination with our spectroscopic parameters to derive homogeneous masses, radii, and ages for all targets.

In this work, we homogeneously measure stellar parameters for BEBOP’s primary stars, using the same methodology overall with consistent input data. We analyse high-resolution spectra to derive the effective temperature (T_{eff}), surface gravity ($\log g_*$), metallicity ($[\text{Fe}/\text{H}]$), and projected rotational velocity ($v \sin i_*$) of each star. We then use these parameters to derive stellar physical parameters such as mass (M_*), radius (R_*), and stellar age. These homogeneous parameters are of interest to produce accurate secondary star masses and radii as part of the EBLM survey (Triaud et al. 2017), and accurate circumbinary masses in the context of the BEBOP survey (Martin et al. 2019). The paper is structured as followed: In Section 2 we introduce the BEBOP sample and in Section 3 the spectroscopic data. Our analysis method is described in Section 4 with results in Section 5. Finally, we conclude in Section 6.

2 THE BEBOP SAMPLE

A total of 179 systems are analysed in this paper with a magnitude range $m_v = 8.31$ to $m_v = 12.96$ (see Fig. 1). The sample is split into a Northern sample (93 systems observed with the SOPHIE spectrograph, see Section 3.1) and a Southern sample (110 systems observed with HARPS, see Section 3.2). A total of nine systems are common between the Northern and Southern samples, selected on purpose in order to compare the sensitivity of both instruments to

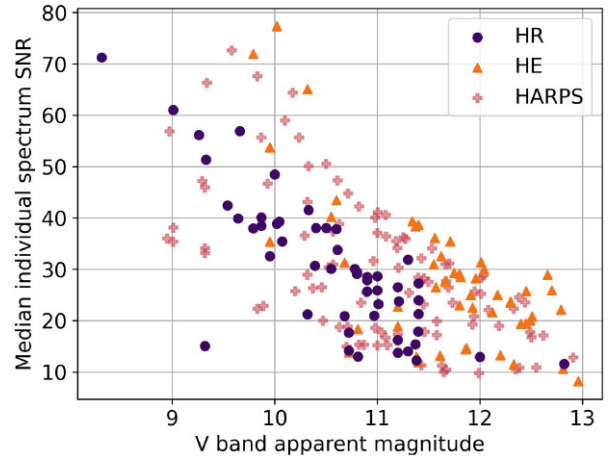


Figure 1. The median SNR of individual spectra is plotted against the apparent V-band magnitude for each BEBOP sample target. The North Sample data are split into the two observation modes available with SOPHIE. The HR mode is shown as purple circles, and the HE mode as orange triangles. The South Sample, coming from HARPS, is shown as pink crosses. Note here that HARPS spectra have, on average, a shorter exposure time – this plot should not be taken as a representation of the instrumental performance.

circumbinary exoplanets. This particular subsample is used to cross calibrate the spectroscopic parameters produced by both instruments.

2.1 BEBOP-South sample

The BEBOP-South sample was defined first. All systems identified as part of the EBLM sample (see Triaud et al. 2013, 2017) were considered. Those EBLM secondaries were identified as transiting exoplanet false positives during the WASP survey (Wide Angle Search for Planets; Pollacco et al. 2006; Triaud 2011) thanks to the CORALIE spectrograph (Udry et al. 2000). All had received at least 13 spectra and some many more (e.g. Martin et al. 2019). The BEBOP sample was selected to maximize RV precision and minimize the contribution of the secondary stars. All visually identified double-lined binaries within the CORALIE spectra were removed. A Keplerian model was adjusted to all systems to obtain preliminary masses for the secondaries. All systems with binary period $P_{\text{bin}} > 4.1$ days (because no circumbinary has been found where $P_{\text{bin}} < 5$ days; Martin 2018), where the variance in the span of the bisector slope of individual spectra (as defined in Queloz et al. 2001) is below 177 m s^{-1} and where the full width at half-maximum of the absorption lines is below 28 km s^{-1} , were kept (both to maximize RV precision and improve sensitivity to circumbinary exoplanets). This resulted in a sample of 56 eclipsing binaries, all expected to have a $\Delta V_{\text{mag}} > 4$ between primary and secondary stars.

In addition, we selected 22 systems identified as likely EBLMs by the KELT survey (Kilodegree Extremely Little Telescope; Pepper et al. 2012; Collins et al. 2018) with $\delta < +10^\circ$, $P_{\text{bin}} > 5$ days, with spectral types later than F4, and $V < 10.5$ for F-types, $V < 11$ for G-types and all K-types. Typically orbital parameters for these systems were more poorly determined than for the EBLM sample.

Finally, since *TESS* was launched (*Transiting Exoplanets Survey Satellite*; Ricker et al. 2014), 32 new eclipsing systems consistent with EBLMs were added in 2021. These are typically brighter than the original EBLM sample, but usually without any prior RV information except in rare cases such as TOI-222 (Lendl et al. 2020).

Their other properties, such as P_{bin} , are consistent with the rest of the sample.

2.2 BEBOP-North sample

The EBLM project's northern counterpart used SuperWASP to find candidates, and then SOPHIE to identify EBLM false positives (e.g. Gómez Maqueo Chew et al. 2014). However, observations and classifications were not as systematic as in the South. As such, the BEBOP-North sample was selected first from the KELT catalogue (Collins et al. 2018), cross-matched with SuperWASP/SOPHIE observations for confirmation. In addition, all SuperWASP/SOPHIE false positives were reviewed selecting likely EBLMs from the eclipse depth and the absence of visible secondary eclipses. As in the South, only binaries with $P_{\text{bin}} > 5$ days, with spectral types later than F4, were kept. Only objects in the Northern hemisphere ($\delta > 0^\circ$) were selected, resulting in a sample of 120 systems. A first reconnaissance campaign was conducted on SOPHIE in 2018 to remove double-lined binaries and confirm the binary nature of each system, reducing the sample to 93 binaries. First, all systems with $V > 11.5$ were observed with the high-efficiency mode and all others in the high-resolution mode. After a few observations were collected, all systems with line widths $> 15 \text{ km s}^{-1}$ were moved to high-efficiency mode since for those, spectral resolution is not as much of an issue.

In both the Northern and Southern samples, systems were divided into a primary and a secondary sample. Typically, systems in the primary sample have more precisely measured RVs with the goal to collect of order 40 to 50 spectra and detect circumbinary planets. Systems in the secondary sample typically receive of order 10–15 measurements only.

3 OBSERVATIONS

The data set analysed in this paper consists of 4512 high-resolution spectra obtained with the SOPHIE and HARPS spectrographs from 2013 to 2023, the majority of which (70 per cent) were observed with a 1800-s exposure time.

3.1 SOPHIE spectroscopy

The SOPHIE échelle spectrograph (Perruchot et al. 2008; Bouchy et al. 2009) is mounted on the 193 cm reflector telescope at the Haute-Provence Observatory. SOPHIE has a wavelength range from 387.2 nm to 694.3 nm. Two observation modes are available: high-resolution (HR) and high-efficiency (HE), respectively, having resolutions of $R = 75\,000$ and $R = 40\,000$. Using the HE mode allows for a throughput increase equivalent to 1 mag. The versatility of the two modes is well demonstrated in the data set. Out of the 93 targets in the BEBOP Northern sample (taken using the SOPHIE spectrograph), 54 were observed in HE mode and 56 in HR mode (meaning 17 were observed in both modes). The median signal-to-noise ratio (SNR) achieved for individual spectra in the HE mode is 27, and the median SNR for the HR mode is 33. The sample is presented in Fig. 1. When considering the combined spectra used for analysis, the median SNR for the HR mode is 88, and 87 for the HE mode.

All spectra are acquired as an échelle onto a CCD camera. The instrument is calibrated with Tungsten lamps at the start of every night to locate where each spectral order is, as well as to perform a flat field. Biases and darks are also obtained daily. In addition, Thorium–Argon lamps and a Fabry–Pérot etalon are used to establish an accurate wavelength solution. A number of reference stars are

observed every night in both the HR and HE modes to track the stability of the instrument (typically of order 2 m s^{-1} ; Bouchy et al. 2013; Courcol et al. 2015; Hara et al. 2020). Additional Fabry–Pérot calibrations are obtained roughly every 2 h throughout the night.

SOPHIE operates with two fibres. All observations obtained for BEBOP use the `objAB` mode where one fibre is on target and the other is on the sky so as to remove any contamination from e.g. Moonlight. Only one system was observed with the `wavesimult` mode where the second fibre is instead illuminated by a Fabry–Pérot etalon to produce a simultaneous calibration. This mode is usually reserved for systems where the most extreme RV precision is needed, which is not the case for the BEBOP stars. In the case of EBLM J0626+29, however, the sky fibre, which cannot be moved, coincided with another star.

Using the calibration frames, each spectral order is extracted from the CCD by the SOPHIE Data Reduction Software (DRS), producing an `e2ds` file. Each order is corrected for the instrumental blaze function and stitched together to create a one-dimensional spectrum, the `s1d` files, which is what we use for our analysis. Each individual `s1d`'s wavelengths solution is corrected to the barycentre of the Solar system (Bouchy et al. 2009; Courcol et al. 2015).

3.2 HARPS spectroscopy

The HARPS spectrograph is mounted on the ESO 3.6 m telescope at La Silla observatory in Chile (Mayor et al. 2003). HARPS has a resolving power $R = 115\,000$ over a wavelength range 378 nm – 691 nm. Individual HARPS spectra used within this paper have a median SNR of 30. Observations and recording of spectra are done in a similar fashion to SOPHIE. Like SOPHIE, HARPS utilizes two fibres, with one on the target and the other used as a calibration – either by use of a Th–Ar reference spectrum, or the sky background.

The data reduction for HARPS follows very closely the method outlined for SOPHIE. The main difference is that we only used the HR mode for observation with HARPS (called HAM). Like for SOPHIE, HARPS can either be used in `objAB` or in `wavesimult` mode. All BEBOP observations used the `objAB` mode except for four systems identified by the *TESS* mission, because their brightness and spectral properties allowed us to reach a photon noise below HARPS's long-term stability (around 1 m s^{-1} ; Fischer et al. 2016) and a simultaneous calibration was necessary to make the best use of the instrument. HARPS is stable enough that neither reference stars nor intra-night calibrations are needed.

The RV of the target spectrum can then be extracted by both the SOPHIE and HARPS reduction pipelines as the mean velocity from a Gaussian fitting to the cross-correlation function (CCF) profile. Out of all BEBOP targets, six were fitted with a K-type mask by the HARPS and SOPHIE data reduction pipelines, with all others being fitted with G-type masks.

Fig. 1 shows the HARPS spectra follow the same general trend as the SOPHIE data in terms of the SNR achieved for individual spectra. After coadding, the median spectral SNR is 126, surpassing that achieved by SOPHIE as outlined in Section 3.1. All targets observed with HARPS were also observed using CORALIE; however, the former was used due to the superior SNR achieved.

4 SPECTROSCOPIC ANALYSIS

Two commonly used methods to retrieve atmospheric parameters via spectral analysis include the curve-of-growth equivalent widths (EW) (e.g. Sousa et al. 2011; Sousa 2014) and spectral synthesis (e.g. Valenti & Piskunov 1996; Adibekyan et al. 2012; Tsantaki et al.

2018) methods. Alternative methods are also used extensively, such as the neural-network based Payne algorithm as used by the SAPP pipeline for the analysis of the PLATO core sample (Gent et al. 2022). The EW method uses the neutral and ionized absorption lines of only one element, resulting in a quick return of parameters. The atomic species used depends on the conditions of the star. For example, for young and/or active stars, it can be beneficial to use titanium (Ti) lines, as described by Baratella et al. (2020). However, for this work we employ the more commonly used Fe I and Fe II lines, which are abundant in the spectra of main-sequence FGK stars.

On the other hand, spectral synthesis is more computationally intensive, iterating through parameters that synthesize a spectrum until the synthesized one matches the observed spectrum. Analyses of large data sets would benefit from the speed of the EW method; however, this method is unable to constrain the projected rotational velocity or macroturbulent velocity since a line's EW is conserved under these broadening parameters (e.g. Sousa et al. 2011; Santos et al. 2013). To provide the most complete stellar information, the synthesis method must also, therefore, be implemented.

For the analysis of the BEBOP survey stars, we combine the strengths of both methods to provide a full and homogeneous analysis of the spectra of these FGK main-sequence stars. We utilize the speed of the EW method to provide excellent initial parameters for the synthesis method, which then runs much quicker. We use the `iSpec` framework (Blanco-Cuaresma et al. 2014; Blanco-Cuaresma 2019) for our analysis. In this section, we describe the details of our analysis and the tests done to ensure reliability of our parameters. In Appendix A, we describe the public python pipeline, PAWS,¹ we wrote around the `iSpec` framework to perform our analysis.

4.1 Data preparation

Barycentric velocity correction, made necessary due the Earth's motion, is performed by the SOPHIE and HARPS reduction pipelines (Lovis & Pepe 2007; Bouchy et al. 2009), resulting in only needing to handle RV corrections in order to shift the BEBOP spectra into the lab frame. To perform the RV correction, an atomic line mask developed from the NARVAL solar spectrum (Aurière 2003) is used as a comparison template, representing the lab frame. A CCF is then used to determine the RV of the target star, which is then corrected for in the individual spectra to shift them into the lab frame.

Consistent continuum normalization is a crucial step to ensuring homogeneity throughout the analysis. Continuum flux in every spectrum is allocated as 1.0, with all spectral features, and therefore analysis, relative to this. To perform the normalization, we use the `fit_continuum` function implemented in `iSpec`. Continuum fluxes are found using a median filter of window size 0.05 nm, and maximum filter of 1.0 nm. Noise is identified by the median filter, then the maximum filter is used to block the fluxes in absorption lines. A model of the continuum is created by fitting a B-Spline of 2 degrees to the spectra, every 5 nm. The spectrum is then normalized by dividing all fluxes by this model.

Individual spectra from the same target are coadded prior to analysis to form one higher-SNR spectrum. Average flux and flux error at wavelength steps of 0.001 nm are taken with a default range of 420–680 nm. Testing yielded no significant differences in results for varying wavelength steps. All BEBOP spectra were treated with the same wavelength range to ensure homogeneity. Spectra from the BEBOP sample are supplied without flux errors; we estimated these

by dividing the flux at each pixel by spectral SNR provided in the FITS headers.

4.2 Line list and model atmosphere

A line list must be input during spectral analysis – this provides a subset of lines in the spectrum that will be used to determine the atmospheric parameters. To ensure homogeneity throughout the analysis, the same line list was employed for both the EWs and synthesis parts of our method. The line list created for the `SPECTRUM` code (Gray & Corbally 1994), built on the NIST Atomic Spectra Database (Ralchenko 2005), was chosen due to its proven success and versatility in FGK dwarf analysis (Blanco-Cuaresma et al. 2014).

Absorption lines selected for analysis in the spectra are identified using a line mask. The line masks provided with `iSpec` contain atomic information inherently dependent on the spectral resolution of $R = 47\,000$ for which they have been optimized. For use for the SOPHIE HE mode spectra, minimal modification was required for this line list, with only 27 lines removed due to consistently performing poorly in chi-squared testing – the wavelengths of these lines can be found in Table B1. HE mode spectra are more at risk of suffering from ‘blended’ lines, in which the shallower and broader lines of the lower resolution spectrum may blend together.

To preserve the higher resolution achieved in the SOPHIE HR and HARPS spectra, we developed new line masks for this work using `iSpec`, which are publicly available on GitHub. For use with the HARPS spectra, we identified line masks using the HARPS-N solar spectra (Dumusque et al. 2021), and the NARVAL solar spectrum at a resolution of $R = 65\,000$ (Aurière 2003) for the SOPHIE HR spectra. Individual abundances were then calculated for each line in these masks – where these were not within 0.05 of the accepted solar values, the masks were discarded to avoid lines that would not be suitable for atmospheric parameter determination. In the case of spectral synthesis, this constraint was extended to within 0.1 dex of solar abundances to allow for more lines to be available for synthesis.

Both analysis methods require a model atmosphere grid to be input. We chose to use the ATLAS9 set of model atmospheres (Kurucz 2005). ATLAS is inclusive of a range of 4500 to 8750 K in T_{eff} , 0.00 to 5.00 dex in $\log g_*$, and -5.00 to 1.00 dex in metallicity. Computation time is saved by the models only working with plane-parallel geometry atmospheres, which assume local thermodynamic equilibrium (LTE) and neglect 3D convection. This assumption breaks down for cold giant and super-giant atmospheres – although on the whole valid for FGK stars, it should be cautioned that biases may be introduced in Fe abundance and should be considered when abundances accurate to a few per cent are desired, as described by Bergemann et al. (2012).

Studies such as those by Cooke et al. (2020) often demonstrate extreme difficulty in constraining $\log g_*$ from SOPHIE HE mode spectra, with that particular study reporting their $\log g_*$ value with a significant error of 0.22 dex. Not only is such uncertainty seen in results from lower-resolution spectra, studies such as those by Torres et al. (2012) also reveal $\log g_*$ determination to be highly problematic in spectra of $R = 46000, 48000, 51000,$ and 68000 . Careful consideration was paid throughout this analysis to the fact that the spectroscopic $\log g_*$ values derived for the BEBOP targets may be less reliable than those obtained via other methods such as photometry or via independently derived stellar mass and radius.

4.3 Analysis process

Using either the EW or synthesis methods can produce reliable results. In this section, we discuss a robust approach that allows

¹<https://github.com/alixviolet/PAWS>

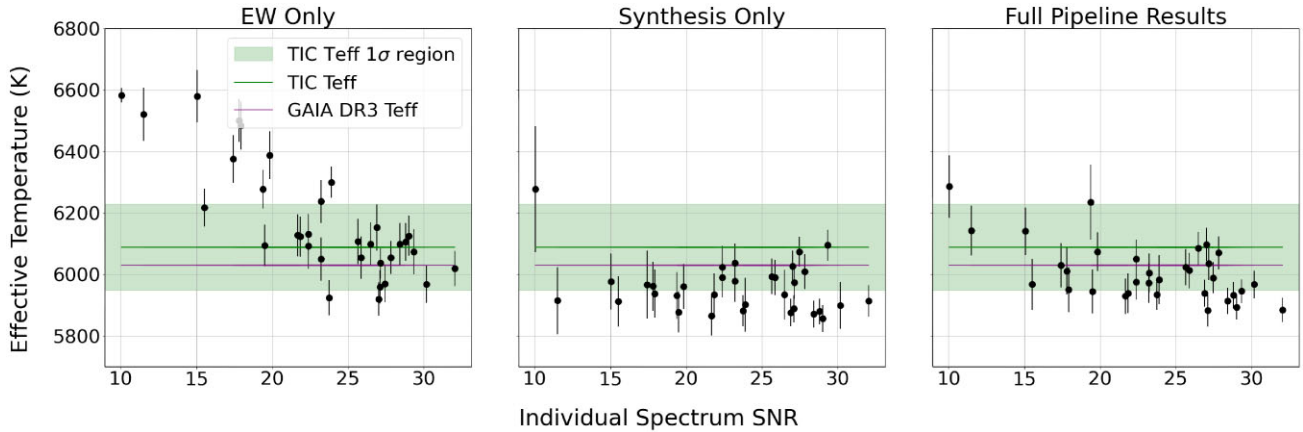


Figure 2. Across all three panels, the TIC T_{eff} value for J0002+47 is represented by the green horizontal line, with its error bars shown as the green shaded region. The purple horizontal line represents the *Gaia* DR3 T_{eff} , supplied without errors. (a) T_{eff} derived from varying SNR spectra of J0002+47 using only the equivalent widths method. (b) Effective temperature derived from varying SNR spectra of J0002+47 using only the synthesis method. (c) T_{eff} derived from varying SNR spectra of J0002+47 using both methods subsequently.

us to adopt both methods in an homogeneous way. Atmospheric parameters are first derived via the EW method, however due to this method’s inability to constrain $v \sin i_*$ and v_{mac} this does not obtain the full set of desired parameters. These results are thus used as initial parameters for the synthesis method, which derives the final set of atmospheric parameters.

4.3.1 Equivalent widths

We first use the EW method, employing only the Fe I and Fe II lines from the line list. We fit a Gaussian profile to each spectral line separately using *ARES* (Sousa et al. 2015). The equivalent width is defined by taking a rectangle with a height equal to that of the continuum, and varying the width of it until the rectangular area is equal to that of the line under the continuum. The *WIDTH* radiative transfer code (Sbordone et al. 2004) then derives individual abundances for these Fe lines based on a set of initial atmospheric parameters – in this work, these were set to the solar values collated in Blanco-Cuaresma (2019) since the BEBOP targets were chosen to be FGK dwarfs.

Through a minimization procedure, stellar parameters are then varied with the best-fitting parameters ensuring ionization and excitation balance. We fit for T_{eff} , $\log g_*$, and $[\text{Fe}/\text{H}]$. v_{mic} is estimated using the *estimate_vmic* function included in *iSpec*; this relation depends on T_{eff} , $\log g_*$, and $[\text{Fe}/\text{H}]$, and was derived using the results of GES (*Gaia*-ESO Survey) UVES data release 1 (Blanco-Cuaresma et al. 2014; Jofré et al. 2014).

4.3.2 Spectral synthesis

Unlike the EW method, spectral synthesis uses every line in our line list. The *WIDTH* radiative transfer code is not able to perform spectral synthesis, so this part of the pipeline calls upon the *SPECTRUM* code (Gray & Corbally 1994), chosen due to proven speed and reliability in the analysis of FGK dwarf stars by Blanco-Cuaresma (2019). Stellar atmospheric parameters are used with *SPECTRUM* to generate a synthesized spectrum. Parameters are iterated and used in conjunction with a minimization algorithm to determine the optimal fit of the synthesized spectrum to the observed one. T_{eff} , $\log g_*$, $[\text{Fe}/\text{H}]$, and $v \sin i_*$ are fitted for, whereas v_{mic} and v_{mac} are calculated

using *estimate_vmic* and *estimate_vmac*, with the relation for v_{mac} again based upon the GES UVES results as described for v_{mic} in Section 4.3.1.

The synthesis process is sensitive to its initial conditions. We therefore use the EW method to set reasonable estimates for the first iteration. This ensures that the synthesis begins in a parameter space that reflects the observed spectrum, saving considerable time compared to if beginning from a solar input for all targets. We set the maximum number of iterations to 6; Blanco-Cuaresma et al. (2014) details how this is the optimal number as more iterations can cause metallicity dispersion to be favoured disproportionately compared to other parameters. The errors on derived parameters are calculated using the covariance matrix generated by the least-squares fitting (Blanco-Cuaresma et al. 2014). In the case of T_{eff} , the precision errors reported by *iSpec* are smaller than the expected accuracy of model atmospheres. To compensate for this, the errors are inflated by adding 100 K in quadrature to better reflect the uncertainty (Tayar et al. 2022).

4.4 Handling low SNR data

Since the SNR of spectra is known to be a critical aspect in stellar analysis, we analysed the individual results of using varying SNR spectra for the same target. Such testing was aimed primarily at producing an SNR filter value, under which spectra are not used. Sousa et al. (2008a) state that 90 per cent of their spectra surpass an SNR of 200 for their EW analysis; suggesting this filter would mainly be in place for the first step of our method. We made use of the target EBLM J0002+47, with the primary star being a slow-rotating F-type dwarf. The target has 33 spectra available with a large range of SNR, observed using the SOPHIE HR mode. Individual spectra are not combined as part of this testing; instead the EW and synthesis methods are applied separately using solar input parameters to each spectrum.

The results of using only the EW method are shown in Fig. 2(a), shown as the derived T_{eff} for each individual spectrum plotted against its SNR. Included within the plot is a comparison to literature T_{eff} values for the target, with the TESS Input Catalogue (TIC) value (Stassun et al. 2019) represented in green with the appropriate error range of 140 K, and the *Gaia* DR3 value represented in purple (Gaia Collaboration et al. 2016, 2022; Babusiaux et al. 2023). Although

Table 1. Results of our analysis on EBLM J2046+06 from SOPHIE HR mode and HARPS spectra, compared to results from Swayne et al. (2021) and *Gaia* DR3 (Recio-Blanco et al. 2023).

Source	T_{eff} (K)	$\log g_*$ (dex)	[Fe/H] (dex)	v_{mic} (km s $^{-1}$)
Swayne et al. (2021)	6302 \pm 70	3.98 \pm 0.11	0.00 \pm 0.05	1.61 \pm 0.05
HARPS	6314 \pm 114	4.03 \pm 0.13	-0.10 \pm 0.09	1.84 \pm 0.03
SOPHIE	6231 \pm 105	3.92 \pm 0.15	-0.11 \pm 0.07	1.67 \pm 0.06
<i>Gaia</i> DR3 GSP-Spec	6149 \pm 53	4.08 \pm 0.04	-0.13 \pm 0.04	-

lower than the TIC value, the *Gaia* DR3 T_{eff} (shown as the purple horizontal line) falls within the TIC T_{eff} errors. A very clear trend is displayed, showing a clear deviation from literature T_{eff} decreasing as spectral SNR increases, as one would expect. An SNR of 20 marks a significant cut-off, above which the majority of results lie within the accepted range of the TIC T_{eff} value. To ensure deviations such as those shown in this plot are kept to a minimum, individual spectra with SNR < 20 were filtered out prior to analysis. The RMS deviation (RMSD) from the TIC value using all results EW-only testing is 208 K, whereas after removing spectra with SNR < 20 decreases the RMSD to 91 K – a significant improvement. An additional concern is displayed in the lowest SNR spectrum of Fig. 2(a) having the smallest error in T_{eff} ; this suggests that the error derived for low SNR spectra by only the EW method does not accurately reflect the uncertainty of the value. Indeed, these uncertainties are statistical only and do not reflect all systematic effects involved in the parameter determination as they are not intended to be the final product of the method. Additionally, the uncertainties determined from only the EW method are highly sensitive to the flux errors supplied (Blanco-Cuaresma et al. 2014) – if these were estimated incorrectly, the uncertainties would be affected.

Fig. 2(b) shows the result of using only the synthesis method on the individual spectra of J0002+47. No obvious trend is observed in the T_{eff} values derived with respect to the spectral SNR. Instead, a systematic underestimation of between 50 and 200 K below the TIC T_{eff} is displayed from the majority of spectra. This is likely to be influenced by the solar input parameters used by default with the synthesis method (i.e. when no input parameters are specified), with all results scattered within a much smaller region than in Fig. 2(a). It is interesting that the synthesis method produced an effective temperature within error bars of both literature values using the lowest SNR spectra available, however the lower SNR is reflected by a poorer synthesis fit and thus larger uncertainties. Again investigating the RMSD of the results, the synthesis-only testing has an RMSD of 155 K from the TIC value, greatly reduced compared to the 208 K from EW-only testing. Fig. 2(b) visibly shows much less scatter in the results than Fig. 2(a); if we consider the RMSD from the mean of the results, rather than from the TIC value, a value of 83 K is achieved. This demonstrates the ability of the synthesis method to derive consistent parameters regardless of spectral SNR.

T_{eff} derived by spectral synthesis appears independent of spectral SNR, however indicates an underestimation bias.

Fig. 2(c) demonstrates the benefits of combining both methods. Where the synthesis method displays a bias to its input parameters, and the EW method has particularly poor performance at low SNR, combining the two gives a far lower dispersion of results. Returning to the metric of RMSD from the TIC T_{eff} , using the entire pipeline returns an RMSD of 123 K, the lowest of the three tests. Additionally, the RMSD from the mean T_{eff} determined from the pipeline is 92 K, again showing strong consistency. In fact, all but one of the results agrees with the TIC values. Agreement is stronger with the *Gaia* DR3

effective temperature in Fig. 2(c), as is also reflected in the higher SNR region of Fig. 2(a). No metric is available to determine which value represents the most reliable result, so within this paper they are treated as equally likely. Given that the results in Fig. 2(c) agree largely with both values, there is no cause for concern or necessity to prove one value as more physically correct than the other.

In cases where the SNR of the combined spectrum is extremely low (< \approx 50), we chose to skip the EW step and purely use the synthesis method for analysis. As shown in Fig. 2, the synthesis method is far less affected by low SNR spectra, whereas the EW method can produce results that differ hugely from expectations. We chose to only compare the effective temperatures as photometric metallicity may not be a reliable reference (Morrell & Naylor 2019).

4.5 Handling fast rotators

It is well established that for fast-rotating stars ($v \sin i_* \gtrsim 5 \text{ km s}^{-1}$) the reliability of the EW method is reduced due to the blending of spectral lines (Tsantaki et al. 2014). To deal with this, we adopt the same approach as in Section 4.4, in which the EW method is skipped. The full list of targets for which the EW method was skipped is shown in Table C1. The blending of lines by high rotational velocity manifests as an increased FWHM of the CCF described in Section 4.1, which is essentially the average shape of the spectral lines. The FWHM of the CCF can therefore be used to determine an estimate for the $v \sin i_*$, as detailed by Rainer et al. (2023). Where the FWHM indicates that the star has $v \sin i_* \gtrsim 5 \text{ km s}^{-1}$ (i.e. FWHM $\gtrsim 20 \text{ km s}^{-1}$), only the synthesis method is used in analysis, with solar parameters as inputs, and the initial $v \sin i_*$ set to that estimated from the FWHM.

4.6 Testing on J2046+06

We used EBLM J2046+06 to test the output of our combined method, due to having recent and reliable literature parameters determined spectroscopically by Swayne et al. (2021). Using 22 HARPS spectra combined to an SNR \approx 300, their analysis uses ARES+MOOG, as described by Sousa (2014) and Santos et al. (2013). Differing from our method, they employ only the EW method using the ARES code (Sousa et al. 2007, 2015) together with the line list described in Sousa et al. (2008b), Kurucz model atmospheres (Kurucz 1993), and the MOOG radiative transfer code (Snedden 1973).

Both SOPHIE HR and HARPS spectra are available for EBLM J2046+06, allowing additionally for testing of continuity between different instruments.

Table 1 displays the results of the pipeline testing on both SOPHIE and HARPS spectra, in addition to the parameters determined by Swayne et al. (2021) and *Gaia* DR3 GSP-Spec, determined using spectra from the *Gaia*'s Radial Velocity Spectrometer (RVS) (Recio-Blanco et al. 2023). The higher SNR and resolution achieved by HARPS is demonstrated as an advantage here, being closer to the

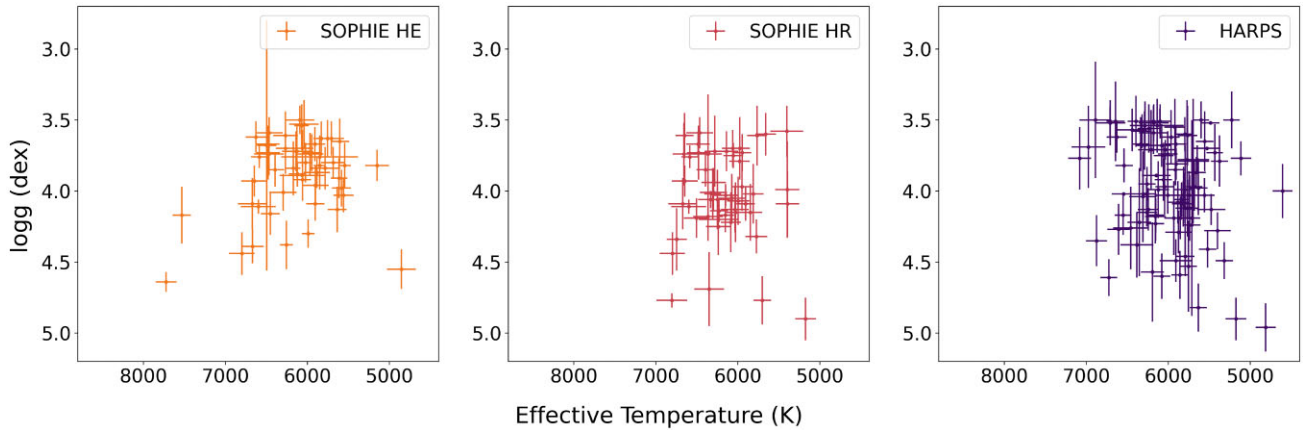


Figure 3. The BEBOP sample presented as a $\log g_*$ versus T_{eff} diagram. The data are split into the respective sources of the spectra, ordered as SOPHIE HE (left), SOPHIE HR (middle), and HARPS (right).

values obtained by Swayne et al. (2021) than those from using the SOPHIE HR mode spectra. With 22 available spectra having an average SNR of 43, the SOPHIE combined spectrum has SNR 131, whereas the HARPS combined spectrum has an SNR of 273, from 27 spectra with average SNR of 57. Despite this, parameters within 2σ are returned in both cases when compared to Swayne et al. (2021) in all cases except v_{mic} . Table 1 displays that atmospheric parameters derived from spectra from different instruments agree well with each other, including for lower SNR and resolution SOPHIE spectra. This strengthens the reliability of our methods. Concerning the results from *Gaia* DR3, our results, and those from Swayne et al. (2021), good agreement is shown.

5 RESULTS

5.1 Atmospheric parameters

We analysed the spectra for all 179 targets in the BEBOP sample with the methods described in Section 4. It took approximately 66 h of computation time.² If a star was analysed using spectra from multiple spectrographs, the final adopted stellar parameters are calculated as an inverse-variance weighted average from the individual results.

The results of the full sample are shown in Fig. 3, in the form of a $\log g_*$ versus T_{eff} diagram. SOPHIE HE mode, HR mode, and HARPS spectra are split into three separate panels on the same scale to demonstrate the dispersion of each.

5.1.1 Comparison with *Gaia* DR3

Gaia DR3 parameters were used in a comparison of our output to literature parameters due to providing results for the majority of our targets. Comparisons were performed for T_{eff} and $\log g_*$, which were consistently available from both GSP-Phot (Andrae et al. 2023) and GSP-Spec (Recio-Blanco et al. 2023). Fig. 4 shows our results versus the *Gaia* DR3 values, with GSP-Spec results limited to those with a `FLUXNOISE` quality flag of Flag 2 or lower, according to appendix C of Recio-Blanco et al. (2023). These results were split into the North and South samples to check for potential instrumental biases. Although error bars are plotted for all points, it is important

to consider that the uncertainties on the *Gaia* DR3 values represent precision values, whereas our T_{eff} were inflated in quadrature.

Fig. 4 shows good agreement between our results and the *Gaia* T_{eff} values. Considering the North sample, the RMSD between our results and GSP-Phot is 199 K; this is smaller than the mean error on our T_{eff} of 256 K. When comparing our results to those from GSP-Spec, the RMSD is 190 K, again being smaller than the mean error. For the South sample, the benefit of the higher resolution manifests in the RMSD between our results and GSP-Phot reducing to 184 K, with a mean uncertainty of 199 K. We see poorer agreement when comparing our results from the South sample to those from GSP-Spec, with the RMSD increasing to 266 K in this case.

Section 4.2 discusses the difficulty in obtaining a reliable value of $\log g_*$ from spectra, hence we did not expect to see concrete agreement when comparing our $\log g_*$ to those from *Gaia* DR3. However, Fig. 4 does show that we do not determine any $\log g_*$ values that would be unphysical for our targets, in addition to showing a general positive correlation between our results and results from *Gaia* DR3. Furthermore, we do not believe the discrepancies to be of great concern in terms of our final results, due to the extensive testing by Mortier et al. (2014) that demonstrates the effect of a changing $\log g_*$ to be insignificant on the derivation of other stellar parameters from spectroscopy.

As discussed by Andrae et al. (2023), *Gaia* GSP-Phot metallicity values suffer from a systematic underestimation. To counteract this, we used the empirical calibration introduced by Andrae et al. (2023) via the python package `gdr3apcal`³ to determine calibrated GSP-Phot metallicities. Fig. 5 shows a comparison of our results with both the results from GSP-Phot and GSP-Spec. Our results have a RMSD from the GSP-Spec values of 0.20 dex, increasing to 0.26 dex when we compare to the GSP-Phot values.

5.1.2 BEBOP colour–magnitude diagram

In Fig. 6, we show the BEBOP sample in a colour–magnitude diagram using *Gaia* DR3 parallaxes, G band apparent magnitudes, and BP-RP colours (Gaia Collaboration et al. 2016, 2023; Babusiaux et al. 2022). No reddening was included so some scatter could arise from that, however, the stars have a mean distance of 336 pc, and reddening would thus be minimal overall. We add a colour bar

²Using 11th Gen Intel Core i7-1185G7@3.00GHz x 8.

³<https://github.com/mpi-astronomy/gdr3apcal>

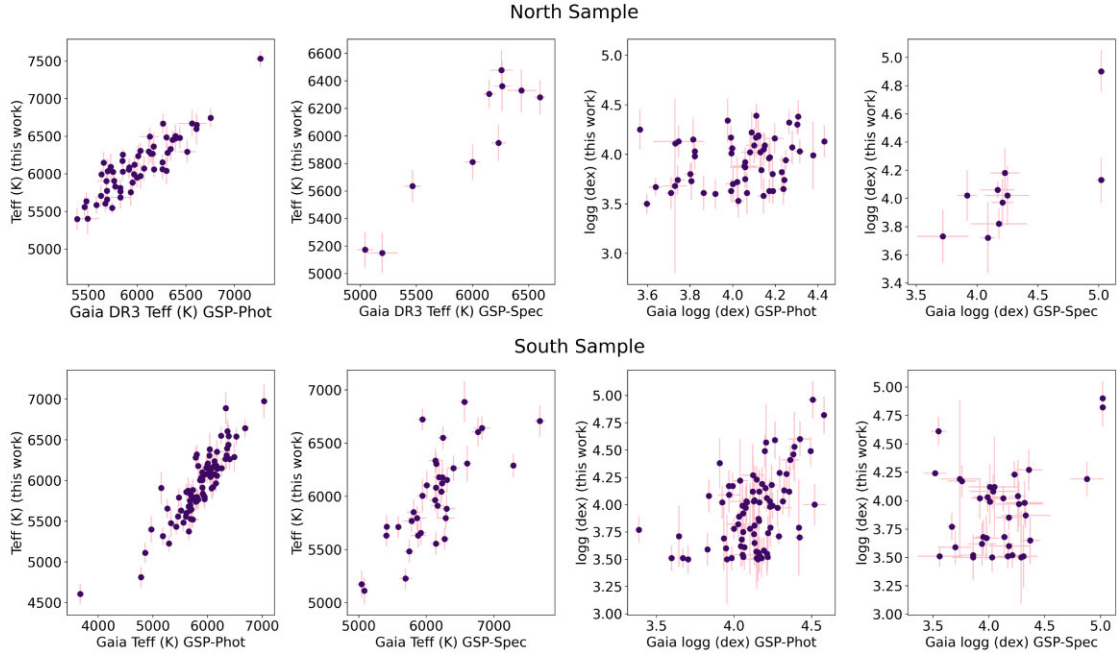


Figure 4. Comparisons of our results (y-axes) to *Gaia* DR3 parameters (x-axes). Results from the North sample (both HE and HR modes) are the top two plots and from the South sample are the bottom two plots, with T_{eff} and $\log g_*$ comparisons on the left and right, respectively.

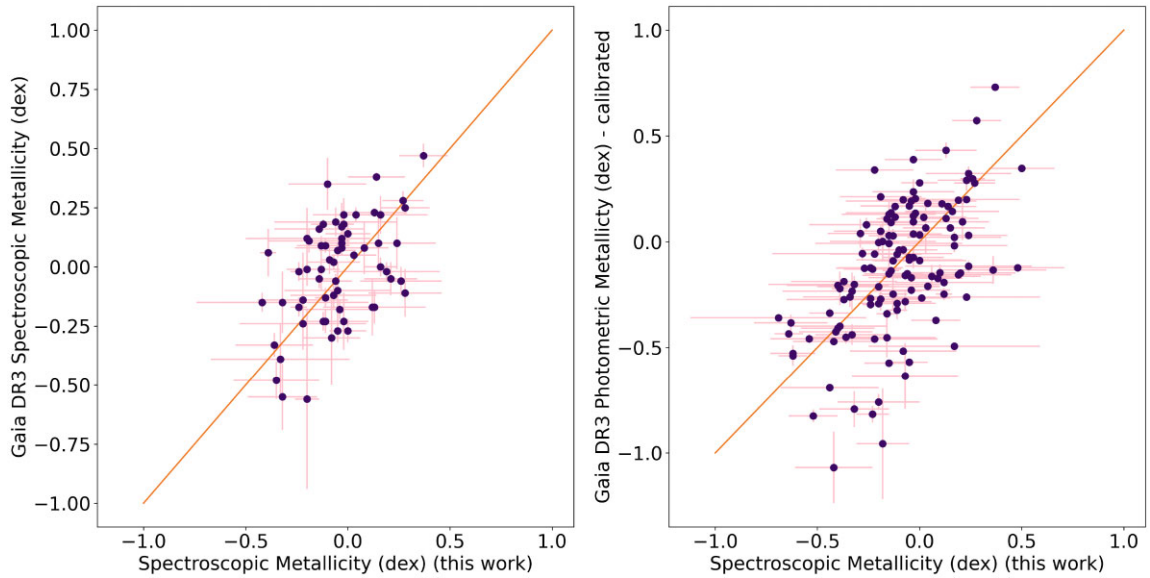


Figure 5. Comparison of metallicities from this work (x-axes) to *Gaia* DR3 GSP-Spec (left) and GSP-Phot (right).

representing our derived effective temperature for each target. As one would expect the sample follows the main sequence with the hottest stars represented in this figure occupying the upper left of the colour–magnitude diagram, being the bluest and brightest from the sample. The reddest and dimmest stars are shown, as expected, to have the lowest effective temperatures.

Ensuring further that the effective temperatures decrease going from bluer to redder stars can present an excellent opportunity to reveal outliers. Fig. 7 separates the data displayed in Fig. 6 into five bins of *Gaia* BP-RP colour, and uses a box-and-whisker plot to show the distribution of effective temperatures in each. Outliers from this are clearly displayed as the red points lying outside of the

whiskers. Beginning with the 0.4–0.6 colour bin, the cool outlier is J0954-45. Our results for this target show a $v \sin i_*$ of $30.01 \pm 16.01 \text{ km s}^{-1}$ – such a high $v \sin i_*$ could have resulted in blended lines that interfered with the analysis. There are no *Gaia* DR3 parameters available for J0954-45, hence we could not do a comparison here. The hotter outlier of the first bin corresponds to J1805+09, which has an exceptionally high $v \sin i_*$ of $49.93 \pm 9.30 \text{ km s}^{-1}$, hence the target is also highly susceptible to blended lines. Our T_{eff} for this target was calculated to be $7532 \pm 111 \text{ K}$; we can compare this to the *Gaia* DR3 T_{eff} of $7267 \pm 49 \text{ K}$, keeping in consideration that *Gaia* DR3 errors are precision-only, whereas we have inflated our T_{eff} uncertainties in quadrature to reflect inaccuracies in the atmospheric models used for

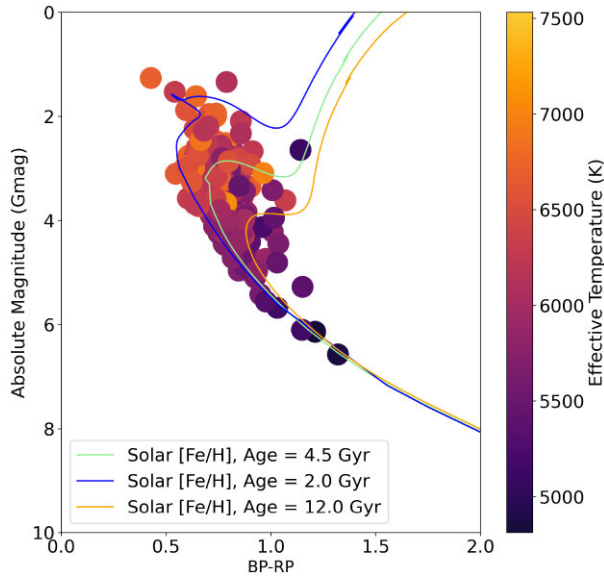


Figure 6. Colour–magnitude diagram of the BEBOP sample, using *Gaia* DR3, with the colour representing our effective temperature. The cooler stars are represented by darker colours, becoming brighter as the effective temperature increases. The expected trend of the brightest, bluest stars (top left) being the hottest, and the dimmer, redder ones (bottom right) being the coolest is seen clearly here.

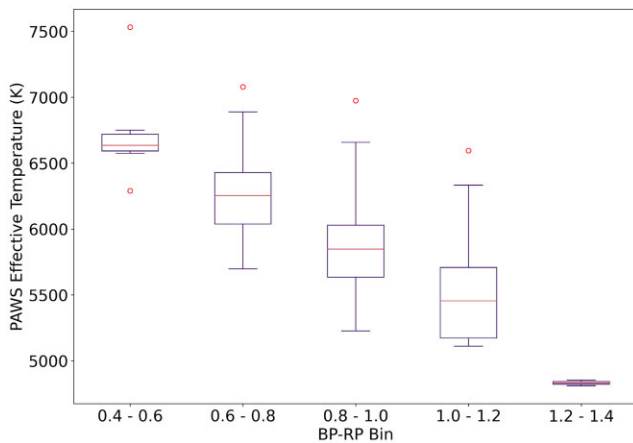


Figure 7. Box-and-whisker plot of the distribution of effective temperatures derived for targets in each *Gaia* DR3 colour bin, as taken from Fig. 6.

analysis. The *Gaia* DR3 result would also place the T_{eff} as an outlier in Fig. 7. Further investigation of this target reveals the TIC radius reported to be $1.68 \pm 0.07 R_{\odot}$ – together with the pipeline-derived effective temperature for the HE mode of 7375 ± 180 K, Pecaut & Mamajek (2013) place this target in the range of late A- to early F-type stars. This indicates a possible unsuitability of J1805+09 as part of an FGK data set. With an HE mode combined SNR of 65, additional observations of the target would be required to reach an SNR of 100 and reduce the uncertainty in parameters.

Moving to the 0.6–0.8 bin, the single outlier displayed is J1258–58. This target has no *Gaia* DR3 results to compare to, and with the combined spectrum reaching an SNR of 136 we do not expect that the results are unphysical. The 0.8–1.0 colour bin also contains a single outlier, being J1916–04. Our result for the T_{eff} of this target is 6974 ± 206 K, which is in agreement with the *Gaia*

DR3 T_{eff} of 7033 ± 32 K – this gives confidence in our results for this target. The final outlier in the 1.0–1.2 colour bin is J0525+26; given that the SNR of the combined spectrum is 42, we would require additional data to determine whether this target is an outlier due to its physical conditions or the quality of the data.

5.2 Masses, radii, and ages

The atmospheric parameters of all BEBOP primaries allow us to derive stellar parameters such as mass and radius using stellar evolution models. We applied MIST isochrones (Choi et al. 2016; Dotter 2016) to interpolate the spectral parameters using the `isochrones` package (Morton 2015). This interpolator utilizes a multimodal nested sampler `multinest` (Feroz & Hobson 2008; Feroz, Hobson & Bridges 2009; Feroz et al. 2019) which allows to sample the input spectral parameters together with photometric and distance information. We used our derived T_{eff} and $[\text{Fe}/\text{H}]$, separating them for each instrument and instrumental mode, together with the *Gaia* DR3 parallaxes (Gaia Collaboration 2022), IR colours W1, W2, and W3 from Allwise (Cutri et al. 2021), and the cross matched NIR 2MASS (Skrutskie et al. 2006) colours H , J , K_s from the same catalogue. We chose not to include a value for $\log g_*$ as an input parameter due to being unable to determine its reliability. As we use a very precise parallax and a variety of magnitudes, it is also not a crucial parameter when fitting isochrones and evolutionary tracks. We fit for stellar mass, radius, age, distance, and extinction (A_V). For each target, we sampled 1000 live points and extract the final parameters as median values from the posterior distributions with the errors representing the 16/84 percentile. Following the methodology outlined by Tayar et al. (2022), noise floors of 5 per cent for masses, 4.2 per cent for radii, and 20 per cent for ages were added to our uncertainties.

As highlighted in both Sections 4.2 and 5.1.1, the spectroscopic $\log g_*$ we derive in this work was not expected to be reliable or physically accurate. Our $\log g_*$ values determined using the MIST isochrones better represent the physical conditions of the star. A comparison of these and the spectroscopic values is presented in Fig. 8.

This comparison is analogous to that by Tsantaki et al. (2013), who saw an underestimated when comparison their spectroscopic $\log g_*$ values to those estimates from parallaxes. From Fig. 8, it is also apparent that the uncertainties on the MIST $\log g_*$ s are greatly reduced compared to the spectroscopic values. Taking into account these higher precisions, and the general consensus of the literature, we would suggest that any further analysis required surface gravities is done using the MIST $\log g_*$ values.

The resulting BEBOP primary mass- T_{eff} diagram, coloured by $[\text{Fe}/\text{H}]$, is shown in Fig. 9. Each point in the plot is coloured by the metallicity of the target – this reveals an abundance of solar-and-higher metallicity targets. It is well established that the occurrence rate of giant planets is increased for metal-rich stars (Sousa et al. 2011). Although not as numerous, many metal-poor targets can also be seen in this plot. These are interesting targets for the study of planet occurrence rates; Mortier et al. (2012) demonstrate that giant planet frequencies around low metallicity stars may not be as diminished as initially expected. Future comparisons of the occurrence rates of giant planets found across the entire range of metallicity targets in the BEBOP sample with those previously studied around single stars would be highly beneficial to theories of planet formation. Having stellar mass values for primary stars in the BEBOP sample will allow for such comparisons to include good constraints on planetary masses.

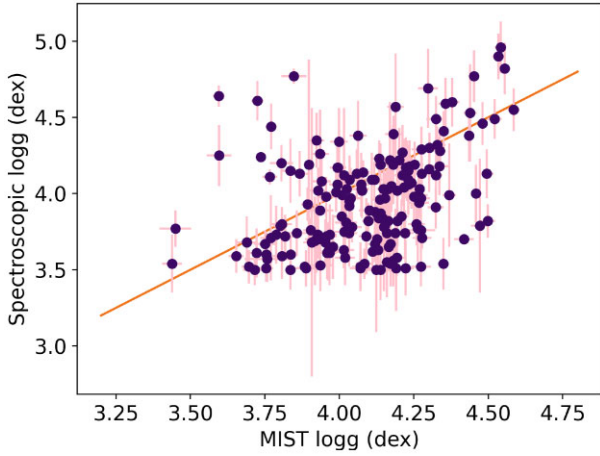


Figure 8. Spectroscopic $\log g_*$ values compared with those inferred from MIST isochrones, both from this work.

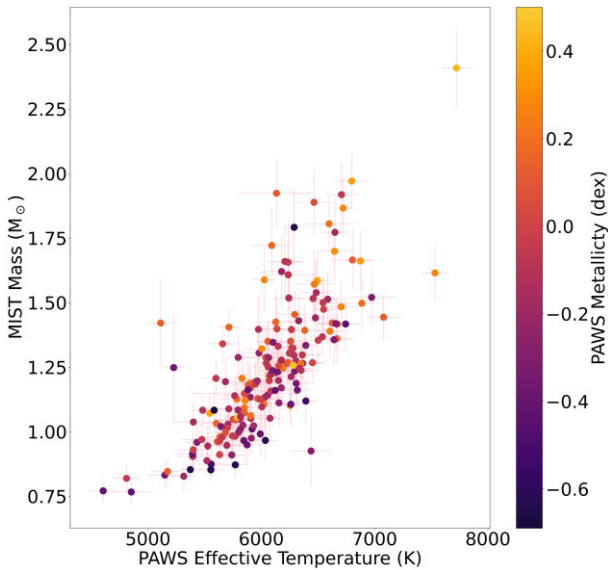


Figure 9. Masses obtained from MIST isochrones plotted against T_{eff} , coloured by the metallicity of each target.

The full set of stellar parameters is presented in an online machine-readable table.

6 CONCLUSION

In this work we present the homogeneous stellar analysis of the BEBOP sample. With effective temperatures ranging from below 5000 K to over 7000 K, the BEBOP sample stretches the limit of what can be achieved with homogeneous analysis. Our spectroscopic method uses the EW method and spectral synthesis in succession to derive all stellar atmospheric parameters, but make use of the computational speed provided by the EW method. We provide a public tool, PAWS, that we used to perform our analysis, but is applicable to any spectra of FGK dwarfs.

Our method has been demonstrated to produce reliable parameters for solar-type main-sequence stars as was the aim during its production, with the advantage of using the EW method to generate initial parameters for spectral synthesis made clear. Although the input parameters do not have a significant impact on the final derived

ones, beginning in a parameter space that is close to the physical one saves on computation time and allows more iterations to be dedicated to the refinement of well-fitting parameters. Comparison to literature parameters for the BEBOP data set revealed strong agreement throughout this work.

Emphasis is put on a minimum SNR of 100, however in this analysis we find no targets deviate significantly from expected results purely due to low SNR despite 93 of 194 spectra not meeting this. The ability to reliably return stellar parameters for spectra of SNR < 100 allows a wide range of spectra to be analysed that may not be possible to use the EW method for. As previously discussed in Section 4.4, EW analyses require high-SNR spectra. Within the BEBOP sample, only 11 per cent of combined spectra reach an SNR of 200, indicating that a pure EW analysis of the sample would not be viable. Poor performance at low SNR indicates that the EW part of our analysis should be skipped for particularly low SNR targets, instead using only synthesis to provide stellar parameters. The use of the EW method in such a scenario is unlikely to initiate the synthesis method in a parameter space reflective of the physical situation. As a result, the time-saving aspect of the EW method would be obsolete here.

Stellar parameters for the BEBOP data set from literature are far from homogeneous. The majority of targets have stellar parameters publicly available from only *Gaia* DR3 and the TIC. Available parameters from these sources are limited, therefore a homogeneous picture of BEBOP targets cannot be created from current literature. In providing essential stellar parameters for every BEBOP target using the same method, with the same inputs, homogeneity is ensured for any further analysis of the BEBOP sample.

ACKNOWLEDGEMENTS

We are grateful to Sergi Blanco-Cuaresma for providing invaluable insights in his code.

We thank the anonymous referee for their insightful and valuable feedback that improved this work.

This paper's results were only possible with the collection of nearly 3000 spectra obtained at two observatories. We therefore particularly thank the staff at ESO's observatory of La Silla and at the Observatoire de Haute-Provence (OHP) for their very kind attention and the extra work they produced during the COVID pandemic, while travel restrictions prevented us from going to the telescopes. This paper is based on data obtained at ESO under proposals 106.212H.001, 106.212H.007, 1101.C-0721(A), 106.21TJ.001, 095.C-0367(A), 092.D-0261(A), 099.C-0138(B), 0101.C-0510(C), 099.C-0138(A), 105.20GX.001, 106.21ER.001, 108.22A8.001, and 0101.C-0407(A) and is based on observations collected at OHP under proposals 19A.OPT.TRIA, 18B.PNP.SANT, 19A.PNP.SANT, 19B.PNP.SANT, 20A.PNP.SANT, 20B.PNP.SANT, 21A.PNP.SANT, 22A.PNP.SANT, and 22B.PNP.SANT.

The authors would like to thank Maria Bergemann for her assistance with some of the spectroscopic analysis that allowed us to refine our methods, and her comment on an earlier version of this paper.

This research has made use of the Exoplanet Follow-up Observation Program (ExoFOP; DOI: 10.26134/ExoFOP5) website, which is operated by the California Institute of Technology, under contract with the National Aeronautics and Space Administration under the Exoplanet Exploration Program.

This work has made use of data from the European Space Agency (ESA) mission *Gaia* (<https://www.cosmos.esa.int/gaia>), processed

by the *Gaia* Data Processing and Analysis Consortium (DPAC, <https://www.cosmos.esa.int/web/gaia/dpac/consortium>). Funding for the DPAC has been provided by national institutions, in particular the institutions participating in the *Gaia* Multilateral Agreement.

This publication makes use of data products from the Wide-field Infrared Survey Explorer, which is a joint project of the University of California, Los Angeles, and the Jet Propulsion Laboratory/California Institute of Technology, funded by the National Aeronautics and Space Administration.

This research is supported from the European Research Council (ERC) under the European Union's Horizon 2020 research and innovation programme (grant agreement no. 803193/BEBOP), and by a Leverhulme Trust Research Project Grant (no. RPG-2018-418).

AVF acknowledges the support of the IOP through the Bell Burnell Graduate Scholarship Fund.

ACC acknowledges support from STFC consolidated grant numbers ST/R000824/1 and ST/V000861/1.

MRS acknowledges support from the UK Science and Technology Facilities Council (ST/T000295/1).

PM and NM were supported by STFC grant number ST/S001301/1.

EM acknowledges funding from FAPEMIG under project number APQ-02493-22 and research productivity grant number 309829/2022-4 awarded by the CNPq, Brazil.

This project has received funding from the European Research Council (ERC) under the European Union's Horizon 2020 research and innovation programme (project SPICE DUNE, grant agreement no. 947634).

DJA is supported by UKRI through the STFC (ST/R00384X/1) and EPSRC (EP/X027562/1).

JRF acknowledges the support of a University of Leicester College of Science and Engineering Studentship. The authors would like to thank Adam Green in his work towards the eclipsing binary sample.

Support for this work was provided by NASA through the NASA Hubble Fellowship grant #HF2-51464 awarded by the Space Telescope Science Institute, which is operated by the Association of Universities for Research in Astronomy, Inc., for NASA, under contract NAS5-26555

AC acknowledge funding from the French ANR under contract number ANR18CE310019 (SPiASH). This work is supported by the French National Research Agency in the framework of the Investissements d'Avenir program (ANR-15-IDEX-02), through the funding of the 'Origin of Life' project of the Grenoble-Alpes University.

EW acknowledges support from the ERC Consolidator Grant funding scheme (project ASTEROCHRONOMETRY, grant agreement no. 772293 <http://www.asterochronometry.eu>)

IB thanks the support of the Programme National de Planétologie (PNP) of INSU,CNRS co-funded by CNES.

DATA AVAILABILITY

All underlying data are available either in the appendix/online supporting material or will be available via VizieR at CDS. All spectra analysed in this paper are either already publicly available on the OHP and ESO archives respectively or will be upon publication of this paper. PAWS is available on GitHub⁴ along with our updated line masks and detailed in Appendix A.

⁴<https://github.com/alixviolet/PAWS>

REFERENCES

- Adibekyan V. Z., Sousa S. G., Santos N. C., Delgado Mena E., González Hernández J. I., Israelian G., Mayor M., Khachatryan G., 2012, *A&A*, 545, A32
- Andrae R. et al., 2023, *A&A*, 674, A27
- Aurière M., 2003, in Arnaud J., Meunier N. eds, EAS Publications Series Vol. 9, p. 105
- Babusiaux C. et al., 2023, *A&A* 674 A32
- Baratella M. et al., 2020, *A&A*, 634, A34
- Bergemann M., Lind K., Collet R., Magic Z., Asplund M., 2012, *MNRAS*, 427, 27
- Blanco-Cuaresma S., 2019, *MNRAS*, 486, 2075
- Blanco-Cuaresma S., Soubiran C., Heiter U. et al., 2014, *A&A*, 569, A111
- Bouchy F. et al., 2009, *A&A*, 505, 853
- Bouchy F., Díaz R. F., Hébrard G., Arnold L., Boisse I., Delfosse X., Perruchot S., Santerne A., 2013, *A&A*, 549, A49
- Buchhave L. A. et al., 2014, *Nature*, 509, 593
- Choi J., Dotter A., Conroy C., Cantiello M., Paxton B., Johnson B. D., 2016, *ApJ*, 823, 102
- Collins K. A. et al., 2018, *AJ*, 156, 234
- Cooke B. F., Pollacco D., Almléay Y. et al., 2020, *AJ*, 159, 255
- Courcol B. et al., 2015, *A&A*, 581, A38
- Cutri R. M. et al., 2021, VizieR Online Data Catalog. p. II/328
- Dotter A., 2016, *ApJS*, 222, 8
- Dotter A., Chaboyer B., Jevremović D. et al., 2008, *ApJS*, 178, 89
- Doyle L. R., Carter J. A., Fabrycky D. C. et al., 2011, *Science*, 333, 1602
- Dumusque X. et al., 2021, *A&A*, 648, A103
- Faria J. P. et al., 2022, *A&A*, 658, A115
- Feroz F., Hobson M. P., 2008, *MNRAS*, 384, 449
- Feroz F., Hobson M. P., Bridges M., 2009, *MNRAS*, 398, 1601
- Feroz F., Hobson M. P., Cameron E., Pettitt A. N., 2019, *Open J. Astrophys.*, 2, 10
- Fischer D. A. et al., 2016, *PASP*, 128, 066001
- Gaia Collaboration 2022, VizieR Online Data Catalog. p. I/355
- Gaia Collaboration et al., 2016, *A&A*, 595, A1
- Gaia Collaboration et al., 2023, *A&A* 674 A1
- Gaia Collaboration et al., 2023, *A&A*, 674, A1
- Gent M. R. et al., 2022, *A&A*, 658, A147
- Gómez Maqueo Chew Y. et al., 2014, *A&A*, 572, A50
- Gray R. O., Corbally C. J., 1994, *AJ*, 107, 742
- Hara N. C. et al., 2020, *A&A*, 636, L6
- Jofré P. et al., 2014, *A&A*, 564, A133
- Konacki M., Muterspaugh M. W., Kulkarni S. R., Hełminiak K. G., 2010, *ApJ*, 719, 1293
- Kostov V. B. et al., 2020, *AJ*, 159, 253
- Kurucz R. L., 1993, SYNTH spectrum synthesis programs and line data.
- Kurucz R. L., 2005, Mem. Soc. Astron. Ital. Suppl., 8, 14
- Lendl M. et al., 2020, *MNRAS*, 492, 1761
- Lovis C., Pepe F., 2007, *A&A*, 468, 1115
- Martin D. V., 2018, in Deeg H. J., Belmonte J. A., eds, *Handbook of Exoplanets*. p. 156,
- Martin D. V., Triana A. H. M. J., Udry S. et al., 2019, *A&A*, 624, A68
- Mayor M. et al., 2003, *The Messenger*, 114, 20
- Morrell S., Naylor T., 2019, *MNRAS*, 489, 2615
- Mortier A., Santos N. C., Sozzetti A., Mayor M., Latham D., Bonfils X., Udry S., 2012, *A&A*, 543, A45
- Mortier A., Sousa S. G., Adibekyan V. Z., Brandão I. M., Santos N. C., 2014, *A&A*, 572, A95
- Morton T. D., 2015, isochrones: stellar model grid package, Astrophysics Source Code Library, record ascl:1503.010
- Pecaut M. J., Mamajek E. E., 2013, *ApJS*, 208, 9
- Pepper J., Kuhn R. B., Siverd R., James D., Stassun K., 2012, *PASP*, 124, 230
- Perruchot S. et al., 2008, in McLean I. S., Casali M. M., eds, *SPIE Conf. Ser. Vol. 7014, Ground-based and Airborne Instrumentation for Astronomy II*. p. 70140J
- Pollacco D. et al., 2006, *Ap&SS*, 304, 253

- Queloz D. et al., 2001, *A&A*, 379, 279
 Rainer M. et al., 2023, *A&A*, 676, A90
 Ralchenko Y., 2005, *Mem. Soc. Astron. Ital. Suppl.*, 8, 96
 Recio-Blanco A. et al., 2023, *A&A*, 674, A29
 Ricker G. R. et al., 2014, in Oschmann J. M. Jr, Clampin M., Fazio G. G., MacEwen H. A., eds, *SPIE Conf. Ser. Vol. 9143, Space Telescopes and Instrumentation 2014: Optical, Infrared, and Millimeter Wave*. p. 914320, preprint (arXiv:1406.0151)
 Santos N. C. et al., 2013, *A&A*, 556, A150
 Sbordone L., Bonifacio P., Castelli F., Kurucz R. L., 2004, *Mem. Soc. Astron. Ital. Suppl.*, 5, 93
 Skrutskie M. F. et al., 2006, *AJ*, 131, 1163
 Sneden C., 1973, PhD thesis, Ph. D. thesis
 Sousa S. G., 2014, in *Determination of Atmospheric Parameters of B*. p. 297
 Sousa S. G., Santos N. C., Israelian G., Mayor M., Monteiro M. J. P. F. G., 2007, *A&A*, 469, 783
 Sousa S. G. et al., 2008a, *A&A*, 487, 373
 Sousa S. G. et al., 2008b, *A&A*, 487, 373
 Sousa S. G., Santos N. C., Israelian G., Mayor M., Udry S., 2011, *A&A*, 533, A141
 Sousa S. G., Santos N. C., Adibekyan V., Delgado-Mena E., Israelian G., 2015, *A&A*, 577, A67
 Standing M. R. et al., 2022, *MNRAS*, 511, 3571
 Standing M. R. et al., 2023, *Nat. Astron.*, 7, 702
 Stassun K. G., Oelkers R. J., Paegert M. et al., 2019, *AJ*, 158, 138
 Swayne M. I., Maxted P. F. L., Triaud A. H. M. J. et al., 2021, *MNRAS*, 506, 306
 Tayar J., Claytor Z. R., Huber D., van Saders J., 2022, *ApJ*, 927, 31
 Torres G., Fischer D. A., Sozzetti A., Buchhave L. A., Winn J. N., Holman M. J., Carter J. A., 2012, *ApJ*, 757, 161
 Triaud A. H. M. J., 2011, PhD thesis, University of Geneva, Astronomical Observatory
 Triaud A. H. M. J. et al., 2013, *A&A*, 549, A18
 Triaud A. H. M. J. et al., 2017, *A&A*, 608, A129
 Triaud A. H. M. J. et al., 2022, *MNRAS*, 511, 3561
 Tsantaki M., Sousa S. G., Adibekyan V. Z., Santos N. C., Mortier A., Israelian G., 2013, *A&A*, 555, A150
 Tsantaki M., Sousa S. G., Santos N. C., Montalto M., Delgado-Mena E., Mortier A., Adibekyan V., Israelian G., 2014, *A&A*, 570, A80
 Tsantaki M., Andreasen D. T., Teixeira G. D. C., Sousa S. G., Santos N. C., Delgado-Mena E., Bruzual G., 2018, *MNRAS*, 473, 5066
 Udry S. et al., 2000, *A&A*, 356, 590
 Valenti J. A., Piskunov N., 1996, *A&AS*, 118, 595
 von Boetticher A. et al., 2019, *A&A*, 625, A150

SUPPORTING INFORMATION

Supplementary data are available at *MNRAS* online.

Please note: Oxford University Press is not responsible for the content or functionality of any supporting materials supplied by the authors.

Table A1. Files saved by PAWS into the target folders and their descriptions.

File name	Description
<i>SNR_list.txt</i>	Text file listing the SNR of all spectra used for coadding, with the last value being the coadded spectrum SNR.
<i>prepared_1_fits</i>	FITS file of the coadded spectrum as flux versus wavelength (nm), including the flux errors.
<i>params_EW.csv</i>	Table of parameters and errors derived only by the equivalent widths method (i.e. those used as synthesis inputs).
<i>used_linemasks.csv</i>	Table of the wavelengths and properties of the iron lines used by the equivalent widths method.
<i>params_synth_pipeline.csv</i>	Table of the final parameters derived by the pipeline.
<i>fitted_line_params.csv</i>	Table of the wavelengths and properties of the lines used in synthesis fitted.
<i>synthesized_spectrum_pipeline.fits</i>	FITS file of the synthesized spectrum as flux versus wavelength (nm).

Any queries (other than missing material) should be directed to the corresponding author for the article.

APPENDIX A: PAWS

To perform our homogeneous analysis, using several functionalities of iSpec, we wrote a python tool, PAWS, to more easily analyse all the spectra. PAWS stands for Parameters Approximated With Synthesis.

PAWS is presented as an interactive GUI that can handle both individual spectra and also perform bulk analysis. It is publicly available as described in Section 4. Minimal inputs are required, namely a folder path, spectral resolution, desired wavelength range, and an initial estimate of spectral type. Input spectra can either be individual spectra from an instrument's reduction pipeline or pre-combined. The GUI is versatile and suitable for a variety of scenarios, with a setup panel providing simple options to allow flexibility of input.

Spectra from differing instruments and observing modes must be sorted into separate folders by the user before input to PAWS. Once PAWS is initiated, individual spectra are corrected for RV to put them in the lab-frame and undergo continuum normalization. Spectra meeting the SNR threshold of 20 established in Section 4.4 after normalization are coadded, with the resulting spectrum stored in the appropriate folder as 'prepared_spectrum.fits'. Initial values of T_{eff} , $\log g_*$, and metallicity are then generated by applying the EW method to this spectrum using the *Run Analysis Stage 1* button in the PAWS GUI. Upon activating *Run Analysis* in the PAWS GUI, the EW parameters are fed as inputs to the synthesis method, with metallicity fixed due to the proficiency of the EW method in using the iron lines. As v_{mic} cannot be determined via spectral synthesis, it was also necessary to fix this to the value determined as detailed in Section 4.3.1. Results of the full analysis are then saved along with the original data. The final results folder includes the files detailed in Table A1.

PAWS has been set up to offer more functionality than used for the analysis of the paper to allow users to make different choices. These changeable options include:

(i) PAWS can also use non-solar input parameters for the EW section, depending on initial knowledge of a target's spectral type. As the majority of BEBOP targets were fitted with G type masks by instrumental data reduction, the solar inputs to the EW method were not changed during their analysis, further adding to the homogeneity of the method. However, allowing for future investigation of a wider variety of targets, K and F type input parameters have been added as an option for PAWS.

(ii) Although recommended to keep this in place to avoid the introduction of contamination to the combined spectrum, the SNR filter can be removed when using PAWS if necessary.

(iii) Depending on the format of the input spectra, it can be selected whether they need to be coadded or to use a pre-coadded spectrum. Continuum normalization will occur regardless.

(iv) The instrumental resolution and wavelength range can be customized to allow for not only the correct resolution to be used but also to ensure that only the desired section of the spectrum is analysed.

APPENDIX B: ADDITIONAL TABLES

Table B1 presents the lines that were removed from the standard iSpec linelist in our analysis.

Table B1. Lines removed from analysis due to poor chi-squared results from SOPHIE HE mode synthesis fitting.

wave_peak (nm)	wave_base (nm)	wave_top (nm)
480.0649	480.061999995742	480.064999995742
500.5712	500.570999995257	500.572999995257
502.9618	502.960999995201	502.9629999952
503.6922	503.690999995183	503.693999995183
510.403	510.402999995025	510.405999995025
531.0686	531.055	531.089
531.2856	531.271	531.306
531.7525	531.73	531.782
531.8771	531.856	531.892
531.9035	531.892	531.913
532.0036	531.991	532.026
532.4179	532.305	532.512
532.5552	532.538	532.58
532.7252	532.705	532.737
532.9138	532.89	532.951
532.9784	532.951	532.986
532.9989	532.986	533.026
534.0447	534.042999994466	534.045999994466
539.7618	539.75899999433	539.76199999433
547.2709	547.267999994153	547.270999994153
549.1832	549.182999994108	549.185999994108
563.8262	563.823999993761	563.826999993761
566.9943	566.993999993686	566.995999993686
578.7919	578.789999993407	578.792999993407
608.5258	608.523999992704	608.526999992704
623.0722	623.07199999236	623.07499999236
675.2707	675.268999991126	675.270999991126

APPENDIX C: SYNTHESIS-ONLY TARGETS**Table C1.** Targets for which the EW step was skipped during analysis, categorized by the reasoning for doing so.

Reason for skipping EW	Targets
Low SNR (<50)	J1916–04, J0709–48, J1246–48, J1126–55, J1757+32, J0211+36, J2303+39, J1623+05, J0641+28, J1558+24
$v \sin i_{\star} \gtrsim 5 \text{ km s}^{-1}$	J1008–29, J0456–74, J1540–09, J0412–44, J0525–55, J0407–23, J0759–69, J0610–56, J1341–30, J0432–33, J1258–58, J0700+09, J0719+25, J0601+37, J0114+54, J1836+27, J0702+42, J0719+10

This paper has been typeset from a $\text{\TeX}/\text{\LaTeX}$ file prepared by the author.